CRYSTAL GROWTH & DESIGN

pubs.acs.org/crystal

Article

Synthesis, Structure, and Tunability of Zero-Dimensional Organic–Inorganic Metal Halides Utilizing the *m*-Xylylenediammonium Cation: MXD_2PbI_6, $MXDBiI_5$, and $MXD_3Bi_2Br_{12}\cdot 2H_2O$

Published as part of a Crystal Growth and Design virtual special issue on Emerging Investigators 2022

Pia S. Klee, Yuri Hirano, David B. Cordes, Alexandra M. Z. Slawin, and Julia L. Payne*

Cite This: https://doi.org/10.1021/acs.cgd.2c00187

Read Online

ACCESS | Metrics & More | Article Recommendations | Supporting Information

ABSTRACT: Over the past decade, the efficiency of photovoltaic devices based on $CH_3NH_3PbI_3$ have dramatically increased. This has driven research efforts in all areas, from the discovery of materials to film processing to long-term device stability studies. Here, we report the synthesis and structure of three new "zero dimensional" organic–inorganic metal halides which use the meta-xylylenediammonium (MXD) cation: MXD_2PbI_6, $MXDBiI_5$, and $(MXD)_3Bi_2Br_{12}\cdot 2H_2O$. The different structures of the new materials lead to compounds with a range of band gaps with $MXDBiI_5$ having the lowest at 2.15 eV. We have explored the tunabilty of $MXDBiI_5$ through halide substitution by preparing a series of samples with composition $MXDBiI_{5-x}Br_x$ and determined the halide content using energy dispersive X-ray spectroscopy. A large range of solid solution is obtained in $MXDBiI_{5-x}Br_x$, resulting in the formation of single-phase materials for bromine contents from $x = 0$ to 3.71 (iodine contents from 1.29 to 5). This highlights the fact that zero-dimensional organic–inorganic halides are highly tunable, in a similar manner to the higher-dimensional perovskite counterparts. Such new materials open up the opportunity for further studies of the physics and optoelectronic properties of these materials.

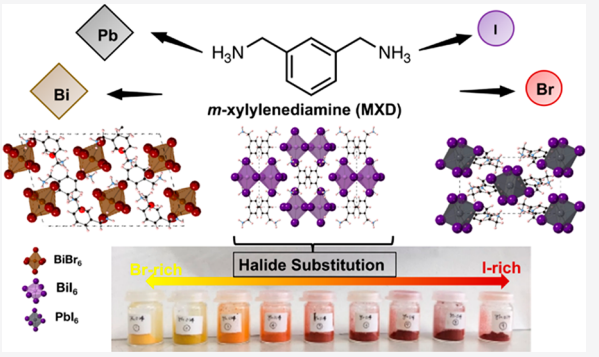

INTRODUCTION

In 2009, Miyasaka and co-workers first tested $CH_3NH_3PbI_3$ and $CH_3NH_3PbBr_3$ in photovoltaic devices.[1] Although the initial efficiencies were modest, the resulting optimization of all aspects of device fabrication has led to groundbreaking photovoltaic power conversion efficiencies.[2−4] Power conversion efficiencies of 25.7% have now been reported for single junction photovoltaics based on $CH_3NH_3PbI_3$ and 29.8% for tandem photovoltaics, based on a combination of silicon and a perovskite layer.[5]

$CH_3NH_3PbI_3$ adopts the perovskite structure, (ABX_3) where A = $CH_3NH_3^+$, B= Pb^{2+}, and X = I^- (or another halide). The structure consists of corner-sharing PbI_6 octahedra, with the organic cation being disordered on the perovskite A-site at room temperature.[6] As the size of the organic ammonium cation is increased, different perovskite-related structure types can form.[7] In particular, layered perovskites based on the Ruddlesden–Popper and Dion–Jacobson structure types have received considerable interest. A notable breakthrough came when a power conversion efficiency of 12.52% was achieved for $(C_4H_9NH_3)_2(CH_3NH_3)_3Pb_4I_{13}$, which adopts the Ruddlesden–Popper structure.[8] Very recently, the "Memory Seed Effect" has been reported, which involves dissolving presynthesized crystals in solvents such as DMF, which enables the preparation of high-quality thin films for a variety of layered perovskites.[9] The solutions have been shown to retain "memory seed" crystallites, which facilitates the production of phase-pure layered perovskites.[9] The use of this "Memory Seed Effect" has led to solar cells with power conversion efficiencies of 17.1% for $(C_4H_9NH_3)_2(CH_3NH_3)_3Pb_4I_{13}$.[9]

Organic–inorganic halide perovskites exhibit great compositional flexibility.[4,10] The A, B, and X sites can be doped in order to fine-tune the electronic structure and band gap for a range of optoelectronic applications.[3,10,11] In particular, as the electronic structure of organic–inorganic metal halides depends on the B-site cation and halide, halide substitution is an excellent way of tuning the band gap of these materials.[12,13] For example, halide substitution in $FAPbI_{3-x}Br_x$ (FA = formamidinium) resulted in the band gap being tuned

Received: February 13, 2022
Revised: April 15, 2022

Table 1. Volumetric Ratios of HBr and HI Used in the Synthesis of the $MXDBiI_{5-x}Br_x$ Mixed Halide Samples

HI	0.00	0.125	0.250	0.375	0.500	0.625	0.750	0.875	1.000
HBr	1.00	0.875	0.750	0.625	0.500	0.375	0.250	0.125	0.000

Table 2. Refinement Details for MXD_2PbI_6, $MXDBiI_5$, and $MXD_2Bi_2Br_{12}\cdot 2H_2O$

	MXD_2PbI_6	$MXDBiI_5$	$(MXD)_3Bi_2Br_{12}\cdot 2H_2O$
CCDC Code	2151572	2151573	2151574
Formula	$C_{16}H_{28}I_6N_4Pb$	$C_{16}H_{28}Bi_2I_{10}N_4$	$C_{24}H_{46}Bi_2Br_{12}N_6O_2$
Formula Weight	1245.01	1963.38	1827.55
Crystal Description	Yellow prism	Red plate	Yellow prism
Crystal Size (mm^3)	0.12 × 0.05 × 0.02	0.15 × 0.06 × 0.01	0.07 × 0.06 × 0.02
Temperature (K)	173(2)	293(2)	173(2)
Crystal System	Monoclinic	Monoclinic	Triclinic
Space group	$P2_1/c$	$I2/m$	$P\bar{1}$
a (Å)	10.9539(3)	8.5380(4)	8.0562(2)
b (Å)	15.5492(3)	11.6966(6)	14.2053(3)
c (Å)	8.8638(2)	19.2708(8)	21.0458(5)
α (deg)			102.611(2)
β (deg)	104.565(3)	99.550(4)	100.779(2)
γ (deg)			99.681(2)
Volume ($Å^3$)	1461.20(6)	1897.82(16)	2253.38(9)
Z	2	2	2
ρ (calc, g/cm^3)	2.830	3.436	2.693
μ (mm^{-1})	12.122	17.407	18.469
F(000)	1104	1696	1668
Reflections collected	18551	6306	39841
Independent reflections (R_{int})	3423 (0.0308)	2302 (0.0324)	10230 (0.0393)
Parameters, restraints	148,48	91, 7	481, 33
Goodness-of-fit on F^2	1.074	1.093	1.091
R_1	0.0179	0.0371	0.0636
R_1 [$I > 2\sigma(I)$]	0.0161	0.0278	0.0398
wR_2	0.0356	0.0680	0.0743
wR_2 [$I > 2\sigma(I)$]	0.0353	0.0645	0.0696
Largest diff. peak and hole ($e/Å^3$)	0.781 and −1.310	0.940 and −1.512	1.706 and −1.458

from 1.48 to 2.23 eV.[3] Unfortunately, photoinduced halide segregation has been reported in $CH_3NH_3PbI_{3-x}Br_x$, yielding iodine- and bromine-rich domains in the thin films.[14] Nevertheless, such tunability of the materials is of interest, particularly in the fields of indoor photovoltaics or tandem solar cells, which can utilize two perovskites with different compositions and band gaps.[4] One method of preventing halide segregation is to use multidentate ligands which create interfaces with a low defect content.[15]

Recently, several new families of layered perovskites have been prepared which incorporate methylammonium in addition to cations which contain aromatic rings such as phenylethylammonium (PEA), 4-aminomethylpyridinium (4AMPY), 3-aminomethylpyridinium (3AMPY), or *meta*-phenylenediammonium (mPDA).[16−18] Several of these perovskites adopt the Dion−Jacobson structure.[16,17] Interestingly, the position of the aminomethyl group on the pyridinium ring in 4AMPY and 3AMPY influences the stacking of the inorganic layer containing lead iodide octahedra and results in a decrease in band gap when going from $(4AMPY)(CH_3NH_3)_{n-1}Pb_nI_{3n+1}$ to $(3AMPY)(CH_3NH_3)_{n-1}Pb_nI_{3n+1}$.[16] $(3AMPY)(CH_3NH_3)_3Pb_4I_{13}$ exhibited a power conversion efficiency of 9.20%. In the $(mPDA)(CH_3NH_3)_{n-1}Pb_nI_{3n+1}$ system, fabrication of phase pure thin films has been challenging for some values of n.[17] $(PEA)_2(CH_3NH_3)_2Pb_3I_{10}$ has been shown to have enhanced moisture stability with respect to $CH_3NH_3PbI_3$.[18]

The term "zero-dimensional perovskite" has been coined for organic−inorganic metal halides which consist of isolated clusters of metal halide octahedra which are separated by organic cations, although strictly speaking these materials do not possess the perovskite structure. Depending on the nature of the metal and halide, different connectivities of octahedra may exist in the cluster, such as isolated MX_6 (where M = metal cation and X = halide) or edge-sharing octahedra to make M_2X_{10} or face-sharing octahedra to make M_2X_9. Zero-dimensional materials are already showing interesting properties; for example, $(1,3\text{-propanediammonium})_2Bi_2I_{10}\cdot 2H_2O$ has been tested as a photodetector, and reproducible photocurrents could be drawn from this material.[19] $(CH_3NH_3)_3Bi_2I_9$ shows highly anisotropic photoluminescence and has shown evidence of quantum cutting.[20] In addition, isovalent doping in the zero-dimensional $(CH_3NH_3)_3Bi_{2-x}Sb_xI_9$ has shown a band-bowing phenomena.[21] Zero-dimensional all-inorganic halides such as A_4PbX_6 and Cs_4SnX_6 (A = K, Cs, Rb and X = Cl, Br, I) are also of interest, particularly for white light emission, and work by Mohammed et al. has recently found that the local octahedral distortions enabled the formation of self-trapped states.[22]

Motivated by reports of enhanced moisture stability when aromatic organic ammonium cations are used,[18] along with the huge compositional and structural diversity of organic−inorganic halides, we have explored the synthesis and tunability of new organic−inorganic halides which use the *meta*-

https://doi.org/10.1021/acs.cgd.2c00187
Cryst. Growth Des. XXXX, XXX, XXX−XXX

Table 3. M−X Bond Lengths and Octahedral Distortions for MX_6 Octahedra in MXD_2PbI_6, $MXDBiI_5$, and $MXD_3Bi_2Br_{12}\cdot 2H_2O$

	MXD_2PbI_6	$MXDBiI_5$	$(MXD)_3Bi_2Br_{12}\cdot 2H_2O$	
M-X(1) (Å)	3.20771(17)	2.9710(5)	2.7942(8)	2.9350(8)
M-X(2) (Å)	3.20776(17)	3.0245(6)	2.8029(8)	2.8073(8)
M-X(3) (Å)	3.21169(17)	3.0565(4)	2.9389(8)	2.8203(8)
M-X(4) (Å)	3.21171(17)	3.0565(4)	2.8813(8)	2.8733(8)
M-X(5) (Å)	3.2443(2)	3.2117(6)	2.8836(8)	2.9270(8)
M-X(6) (Å)	3.2443(2)	3.2459(6)	2.8650(8)	2.7722(8)
Bond length distortion (Δd, $\times 10^{-4}$)[29]	0.258	10.39	8.65	12.98
Bond angle variance (σ^2)[29]	31.63	13.13	18.42	7.46

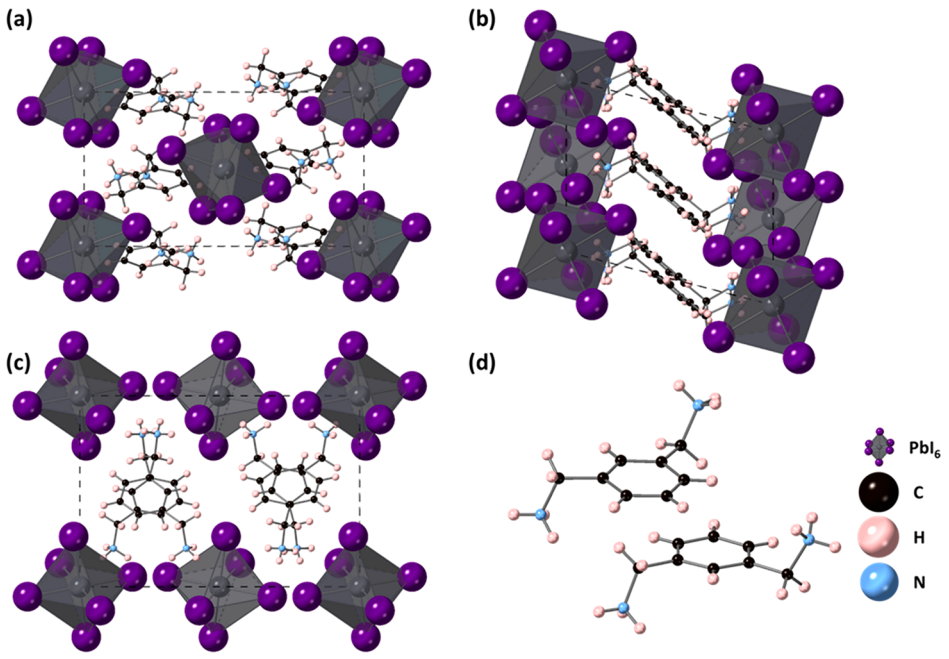

Figure 1. Crystal structure of MXD_2PbI_6 (a) viewed down the *a*-axis, (b) viewed down the *b*-axis, (c) viewed down the *c*-axis, and (d) to show the arrangement of adjacent MXD cations.

xylylenediammonium (MXD, $H_3NCH_2C_6H_4CH_2NH_3^{2+}$) cation.

EXPERIMENTAL SECTION

The synthesis of all materials was based on modifications of the method reported by Poglitsch and Weber for the preparation of $CH_3NH_3PbI_3$.[23] The appropriate metal oxide was dissolved in 5 mL of HX and heated to 80 °C. Separately, 0.5 mL of HX was added to 0.4 mL *m*-xylylenediamine, resulting in the formation of crystals. These crystals were heated until dissolved. The two solutions were mixed and stirred for 30 min. The solution was cooled to room temperature, and the resulting crystals were filtered. The crystals were dried in a vacuum oven at 80 °C for 2 h.

For the synthesis of $MXDBiI_{5-x}Br_x$, 0.47 g Bi_2O_3 was added to a mixture of HX acid (X = Br, I). The volumetric ratio of HI:HBr used in the reactions are given in Table 1. The reaction mixture was then placed on a hot plate and heated to 80 °C, with stirring, until all reactants were dissolved. Then, an equimolar quantity of *m*-xylylenediamine (0.14 mL) was added to the solution, and the mixture was stirred for 30 min. After cooling to room temperature, the crystals were filtered off and left to dry in the fume hood.

Powder X-ray diffraction data were collected on a Panalytical Empyrean Diffractometer using $CuK_{\alpha 1}$ radiation in Bragg−Brentano geometry. Data were collected from 5° to 70° with a step size of 0.017° and a time per step of 0.94 s. PXRD data were analyzed using Topas Academic ver. 6.[24]

Single crystal diffraction data were recorded at either 173 or 293 K using a Rigaku FR-X Ultrahigh brilliance Microfocus RA generator/confocal optics and Rigaku XtaLAB P200 diffractometer [Mo Kα radiation (λ = 0.71073 Å)]. Intensity data was collected using ω steps accumulating area detector images spanning at least a hemisphere of reciprocal space (CrystalClear).[25] The data was processed using CrysAlisPro software.[26] Structure solution was carried out using SHELXT,[27] and structure refinement by full matrix least-squares against F^2 was carried out with SHELXL (2018/3).[28] Non-hydrogen atoms were refined anisotropically, and carbon-bound hydrogens were refined using a riding model. Ammonium hydrogens were located from the difference Fourier map and refined isotropically subject to distance restraints. Selected crystallographic data are presented in Tables 2 and 3. Deposition numbers 2151572−2151574 contains the supplementary crystallographic data for this paper. These data are provided free of charge by the joint Cambridge Crystallographic Data Centre and Fachinformationszentrum Karlsruhe Access Structures service www.ccdc.cam.ac.uk/structures.

Scanning electron microscopy studies were carried out using a JSM IT200 equipped with a 25 mm^2 Jeol DrySD EDS detector and a Jeol JSM 5600. UV−vis diffuse reflectance spectra were collected on a Jasco V650 spectrophotometer equipped with an integrating sphere, in the wavelength range 190−900 nm. $BaSO_4$ was used as a reference.

RESULTS AND DISCUSSION

Crystal Structure. The reactions of MXD with either Bi_2O_3 and HI or HBr, along with PbO and HI, produced the crystalline products $MXDBiI_5$, $MXD_3Bi_2Br_{12}\cdot 2H_2O$, and MXD_2PbI_6. Their structures were determined from single-

https://doi.org/10.1021/acs.cgd.2c00187
Cryst. Growth Des. XXXX, XXX, XXX−XXX

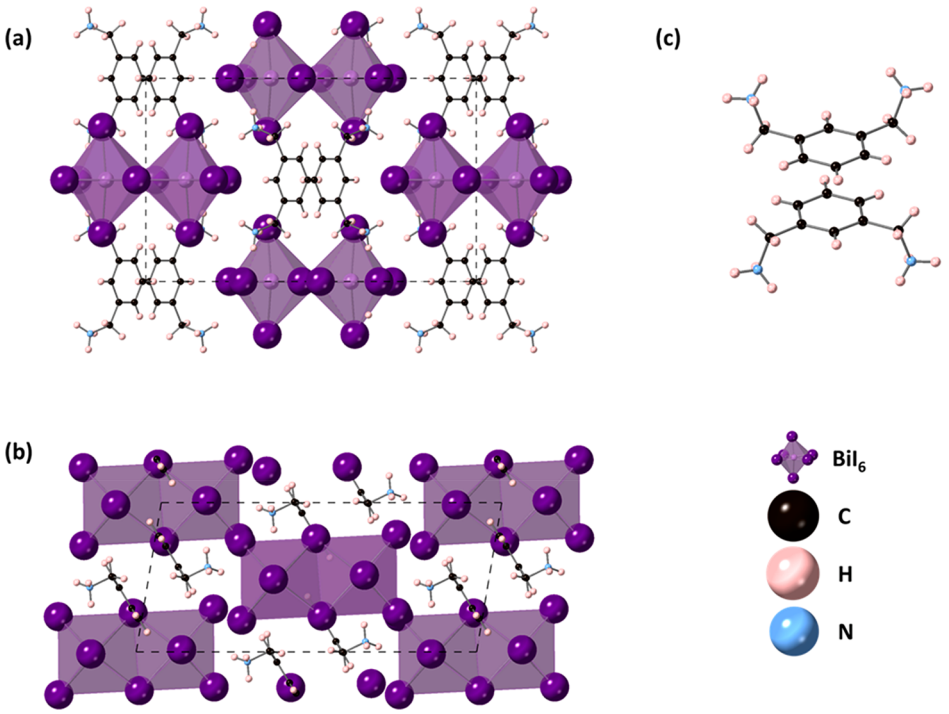

Figure 2. Structure of $MXDBiI_5$ (a) viewed down the *a*-axis, (b) viewed down the *b*-axis, and (c) showing the $\pi-\pi$ stacking arrangement of the MXD cations.

crystal X-ray diffraction data, and selected parameters are tabulated in Table 2.

The structure of MXD_2PbI_6 consists of isolated PbI_6 octahedra separated by MXD cations (Figure 1). Although the structure is not strictly a layered perovskite, the structure can be thought of as a "pseudolayered" material, as the PbI_6 octahedra form layers in the crystal structure but are too far apart to form the corner-sharing-octahedral connectivity required in the perovskite structure. It is likely that this is driven by the ammonium groups from the large MXD cation, which protrude into the inorganic layer. The Pb–I bond lengths range from 3.20774(17) to 3.2443(2) Å (Table 3). The I–Pb–I bond angles range from 81.808(4)° to 98.192(4)° for *cis* I–Pb–I angles, while the *trans* I–Pb–I are 180°. This deviation away from the ideal octahedral angles indicates that the octahedra show some distortion. Such a distortion can be quantified in terms of the bond angle variance and the bond length distortion, as originally reported by Robinson et al.[29] Here, we calculate the bond length distortion to be 0.258 and bond angle variance to be 31.63. The bond angle variance here is much smaller than the 234.2 reported for $(mPDA)PbI_4$ recently reported.[17] The aromatic core of the MXD cation is not directly above adjacent MXD cations but is offset. The orientations of the adjacent MXD cations result in NH_3 groups pointing in three different directions to give a Y-shaped arrangement of the NH_3 groups, with one pair of NH_3 groups being almost eclipsed (Figure 1c). Hydrogen bonds between NH_3 hydrogens and iodine from the PbI_6 octahedra range from 3.546(2) to 3.718(2) Å. Figure S1 shows the PXRD data of the bulk sample. Pawley fits were carried out using the unit cell parameters and space group obtained from single-crystal diffraction. Twelve Chebyshev background parameters, sample displacement, and profile parameters were also refined. The resulting fit is shown in Figure S1, and this confirms the phase purity of the sample.

In contrast to the structure of MXD_2PbI_6, which contains isolated PbI_6 octahedra, the structure of $MXDBiI_5$ consists of BiI_6 octahedra, which share edges to form Bi_2I_{10} dimers (Figure 2). This kind of structural motif has also been observed in other organic bismuth halides.[30,31] The Bi_2I_{10} units are separated by the MXD cations. The Bi–I bond lengths range from 2.9710(5) to 3.2459(6) Å (Table 3). The I–B–I angles range from 171.904(19)° to 178.914(15)° for the iodine in the *trans* positions and from 85.756(15)° to 94.581(17)° in the *cis* position. The Bi octahedra show some distortion, with a bond length distortion of 10.39 and bond angle variance of 13.13. The orientation of the MXD cation plays an important role in holding the structure together. The aromatic rings of adjacent MXD cations are strictly parallel and have a centroid–centroid distance of 3.509(5) Å. The close register of the rings forces the ammonium groups to point to the same side of the ring for each cation, so when considered for each pair of cations, all four NH_3 groups point in opposite directions. The I1–I4 intercluster distance is 4.1357(6) Å, and this is of particular note, as this is comparable to the short interlayer I–I distances of 4.00 and 4.04 Å, which were reported in $(H_3NC_6H_4NH_3)(CH_3NH_3)Pb_2I_7$ and $(H_3NC_6H_4NH_3)(CH_3NH_3)_2Pb_3I_{10}$, respectively.[17] Although these are thought to be the shortest interlayer iodine–iodine distances in Dion–Jacobson perovskites, we note that in zero-dimensional organic–inorganic halides, short intercluster distances of 3.7253(16) Å have been reported in $(H_3NC_6H_4NH_3)_2Bi_2I_{10}\cdot 4H_2O$, while short interchain distances of 3.871(10) Å have been reported in $(H_3NC_6H_4NH_3)Bi_2I_8\cdot I_2$.[17,31,32] Hydrogen bonds between NH_3 hydrogens and iodine in the Bi_2I_{10} units ranged from 3.712(5) to 3.812(6) Å. Figure S2 shows the PXRD data of the bulk $MXDBiI_5$ sample. Pawley fits were carried out using the cell parameters and space group obtained from single crystal diffraction $MXDBiI_5$ and the same nonstructural parameters that were described for MXD_2PbI_6.

https://doi.org/10.1021/acs.cgd.2c00187
Cryst. Growth Des. XXXX, XXX, XXX–XXX

The resulting fit is shown in Figure S2, and this confirms the phase purity of the sample.

The structure of $MXD_3Bi_2Br_{12}·2H_2O$ consists of isolated $BiBr_6$ octahedra, with the asymmetric unit containing two inequivalent $BiBr_6$ octahedra (Figure 3). For the Bi(1) octahedron, the Bi−Br bond lengths range from 2.7942(8) to 2.9389(8) Å, while for the Bi(2) octahedron, the Bi−Br bond lengths range from 2.7722(8) to 2.9350(8) Å (Table 3). In addition, the bond angles of Bi(1) range from 84.45(2)° to 99.54(2)° for *cis* bond angles and 170.57(2)° to 176.29(3)° for *trans* angles, while for Bi(2), the bond angles range from 174.21(2)° to 177.20(3)° for *trans* bond angles and 85.46(2)° to 95.13(2)° for *cis* bond angles. Calculation of the bond length distortion and bond angle variance show that the $BiBr_6$ octahedra exhibit different levels of distortion, with Bi(1) showing the greater angular variance than the Bi(2), while Bi(1) shows less distortion of bond lengths than Bi(2) (Table 3). The bond angle variance of the $BiBr_6$ octahedra are much smaller than that of MXD_2PbI_6, which also contains isolated octahedra (PbI_6) in the structure. They are also significantly smaller than the bond angle variance reported for (mPDA)-PbI_4, but are comparable to those reported for some quinoline and isoquinoline lead halides.[17,33] The shortest hydrogen bonds are formed between the NH_3 and H_2O, with N···O distances of 2.757(12) Å and 2.822(10) Å. Figure S3 shows the PXRD data of the bulk $MXD_3Bi_2Br_{12}·2H_2O$ sample. Pawley fits were carried out using the cell parameters and space group obtained from single crystal diffraction and parameters described for MXD_2PbI_6. The resulting fit is shown in Figure S3, and this confirms the phase purity of the sample. SEM images of MXD_2PbI_6, $MXDBiI_5$, and $MXD_3Bi_2Br_{12}·2H_2O$ are shown in Figure 4.

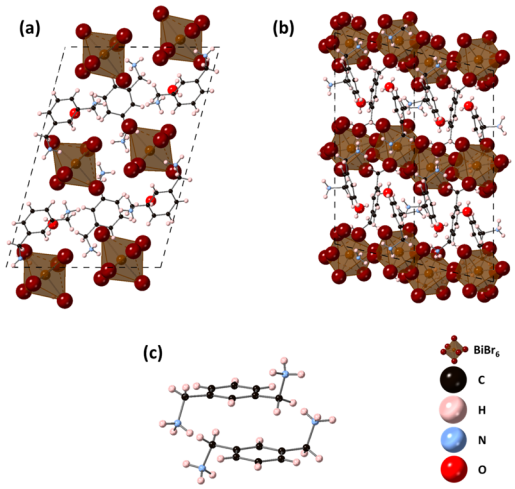

Figure 3. Crystal structure of $MXD_3Bi_2Br_{12}·2H_2O$ (a) viewed down the *a*-axis, (b) viewed down the *b*-axis, and (c) arrangement of adjacent MXD cations.

SEM images of MXD_2PbI_6, $MXDBiI_5$, and $MXD_3Bi_2Br_{12}·2H_2O$ are shown in Figure 4. MXD_2PbI_6 displays aggregates of crystals, with a needle-like morphology, of dimensions of approximately 600 μm by 40 μm. Crystallites of $MXDBiI_5$ also show a needle-like morphology, although the crystals are much shorter than those reported for the MXD_2PbI_6, with dimensions of approximately 50−75 μm by 20 μm. The $MXD_3Bi_2Br_{12}·2H_2O$ sample consists of much thinner crystallites with a narrow, plate-like morphology. A range of crystallite sizes can be observed, with typical dimensions being around 50 μm by 100−200 μm. Although the control of morphology was not considered in this study, this will be of interest in the future, when manufacturing these materials into thin films, as any pinholes in thin films as a result of surface morphology can influence factors such as device performance in photovoltaics or LEDs.

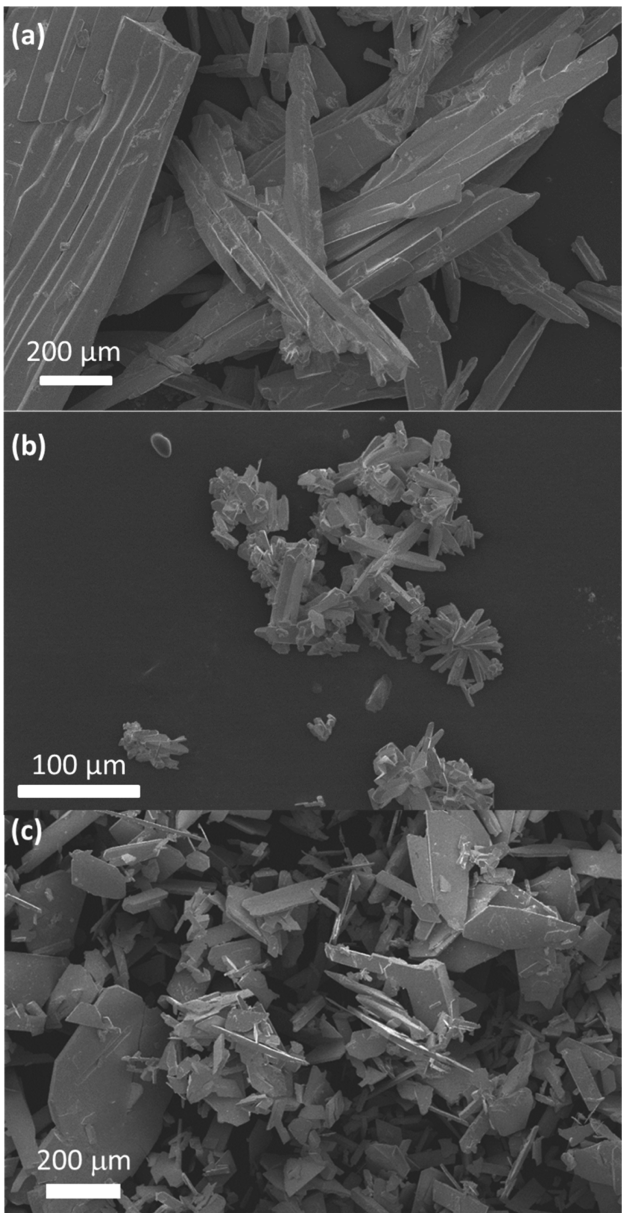

Figure 4. SEM images of (a) MXD_2PbI_6, (b) $MXDBiI_5$, and (c) $MXD_3Bi_2Br_{12}·2H_2O$.

Halide Substitution. It is well-known that the valence band and conduction bands in organic−inorganic halides comprise orbital contributions from both the halide and the inorganic cation.[34] Therefore, isovalent doping on the anion site, e.g., replacing I^- with Br^-, is a particularly useful technique to tune the band gap of the $CH_3NH_3PbI_3$ perovskites.[13,35] This is often termed halide substitution and results in the creation of materials with compositions such as $CH_3NH_3PbI_{3-x}Br_x$. Zero-dimensional inorganic−organic halides commonly exhibit a similar electronic structure to the 3D analogues, but with greater orbital decoupling;[36] therefore, we

https://doi.org/10.1021/acs.cgd.2c00187
Cryst. Growth Des. XXXX, XXX, XXX−XXX

decided to probe halide substitution in $MXDBiI_{5-x}Br_x$, in order to determine the doping limit of Br^- in the $MXDBiI_5$ structure type. A photograph of the $MXDBiI_{5-x}Br_x$ samples is shown in Figure 5 and shows that the color of the samples can be varied

Figure 5. Photograph of halide substituted samples, $MXDBiI_{5-x}Br_x$.

from yellow (Br-rich samples) to dark red (I-rich samples). As these samples were synthesized using solution based-routes, the ratio of I to Br was determined using energy dispersive spectroscopy (EDS) using the SEM. The I:Br ratio in a sample is not the same as the I:Br ratio in its precursor solutions, but across the I:Br ratios studied, the ratio in the sample can be related directly to its ratio in solution (Figure S5).[36] We note that similar phenomena have been reported when two different cations are used in the synthesis of Ruddlesden–Popper phases, as nonstoichiometric ratios of reagents must be used to isolate the phase pure product.[37] In addition, in the synthesis of Cs_2SnX_6 (X = Cl, Br, I) mixed halides, the products were found to be richer in the Cl or Br than would be expected given the ratios in the precursors, and this has been attributed to the difference in solubility of halides in solution.[38]

The PXRD data of $MXDBiI_{5-x}Br_x$ samples are shown in Figure 6, and a representative SEM image of the polycrystalline sample of $MXDBiI_{4.11}Br_{0.89}$ is shown in Figure S5. As can be seen, the 100% Br sample (i.e., "$x = 5$") exhibits a completely different PXRD pattern to the other samples prepared in this series, which indicates that it adopts a completely different structure type, $MXD_3Bi_2Br_{12}{\cdot}2H_2O$ (vide supra). However, with only a small amount of HI in the precursor solution (see Table 1 and Figure S4), the $MXDBiI_5$ structure type is adopted, and all peaks can be indexed to a monoclinic unit cell in space group $I2/m$. This structure type is adopted for all $MXDBiI_{5-x}Br_x$ compositions which have a bromine content, x, between 0 and 3.71 (i.e., having iodine contents from 1.29 up to 5.0). In order to determine the extent of the solid solution in $MXDBiI_{5-x}Br_x$, Pawley refinements were carried out. During the refinements, 12 Chebyshev polynomial terms were used to fit the background, and in addition, unit cell parameters, profile parameters, and specimen displacement were all refined. The resulting variation of unit cell volume with iodine content is shown in Figure 6b, and the corresponding unit cell parameters are plotted in the Supporting Information (Figure S6). As can be seen from Figure 6b, there is a linear relationship between bromine content (x) and unit cell volume, in agreement with Vegard's law, with the exception of a slight leveling off at the lowest bromine contents. This shows that there is a large region of solid solution in the $MXDBiI_{5-x}Br_x$ system. This region of solid solution ranges from a bromine content, x, of 0 to 3.71, and it is likely that a full solid solution could be obtained with further optimization of synthetic conditions. As the bromine content increases, the β angle increases, but there is a leveling off at the highest iodine contents (which corresponds to the lowest bromine contents). The a, b, and c unit cell parameters all show a linear relationship with bromine content and exhibit a smaller leveling off at the lowest bromine contents. The decrease in unit cell parameters with increasing bromine content is expected due to the smaller size of Br^- (1.96 Å) with respect to I^- (2.20 Å).[39]

The Kubelka–Munk transformations of the UV–vis diffuse reflectance spectra of the $MXDBiI_{5-x}Br_x$ samples and $MXD_3Bi_2Br_{12}{\cdot}2H_2O$ are shown in Figure 7, while the MXD_2PbI_6 spectrum is shown in Figure S7. Two absorption features are observed in the spectra for $MXDBiI_{5-x}Br_x$. For $MXDBiI_{5-x}Br_x$, the first feature is in the 2.36–2.06 eV range (corresponding to 525–600 nm) and the second feature is centered around 1.9 eV (~650 nm), while for MXD_2PbI_6, the peak occurs at ~500 nm (2.5 eV) We note that dual features have been observed in both UV–vis spectroscopy and photoluminescence measurements for both 2D, layered materials, and zero-dimensional materials.[40−42] For example, Nag et al. noticed dual-emission in photoluminescence studies of single crystals of $(PEA)_2SnI_4$ (PEA = phenylethylammonium), which was also accompanied by two absorption features in UV–vis absorption spectra of the same material.[41] A similar behavior was also observed for (4-AMP)SnI_4 (4-AMP = (4-aminomethyl)piperidinium).[41] Dual PL emission has also been observed for the zero-dimensional TPA_2SbCl_5 (TPA = tetrapropylammonium).[42] To date, the presence of dual features in the photoluminescence or absorption spectra has been attributed to differences in the edge or bulk of the crystals

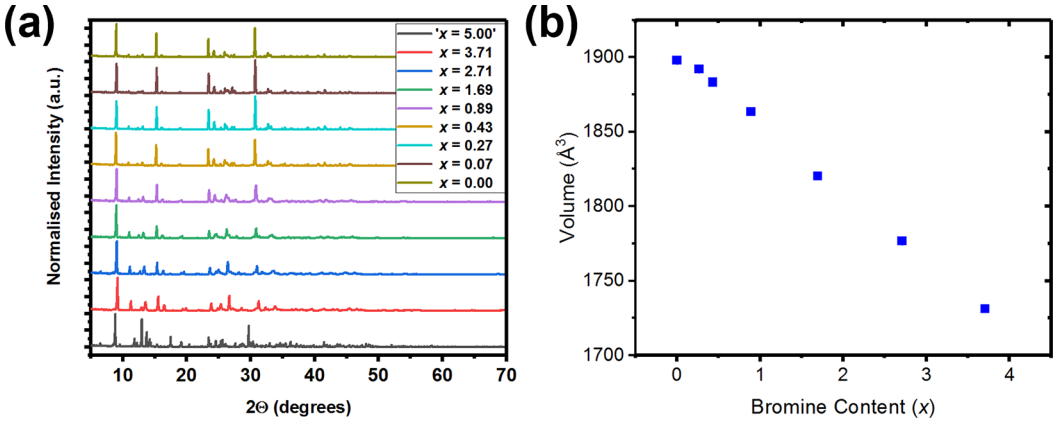

Figure 6. (a) PXRD data of $MXDBiI_{5-x}Br_x$ and (b) variation of unit cell volume with bromine content for $MXDBiI_{5-x}Br_x$. The bromine-end member ($x = 5$) has a different structure type so has been excluded from part b.

https://doi.org/10.1021/acs.cgd.2c00187
Cryst. Growth Des. XXXX, XXX, XXX−XXX

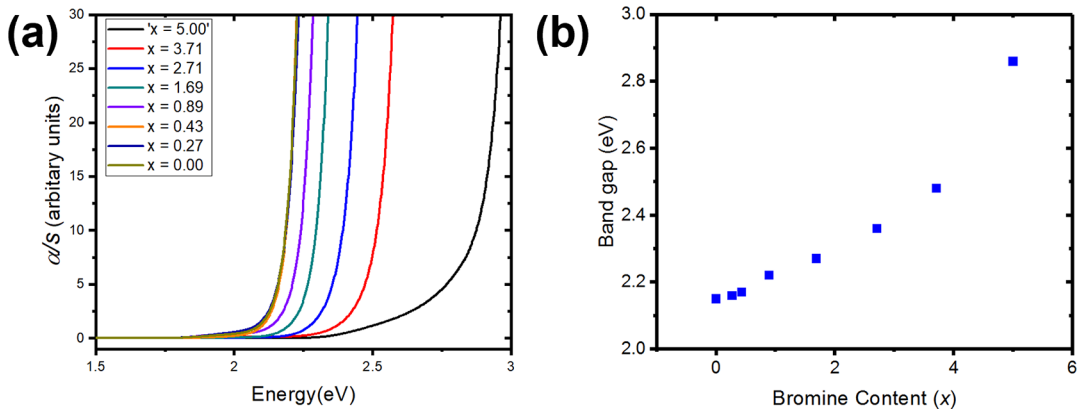

Figure 7. (a) UV−vis diffuse reflectance spectra for $MXDBiI_{5-x}Br_x$ converted using the Kubelka−Munk function ($\alpha/s = (1 - R)^2/2R$) and (b) the variation of band gap with bromine content for $MXDBiI_{5-x}Br_x$. The $x = 5$ sample has a different structure type.

or self-trapped excitons.[41,42] As the bromide content is increased in $MXDBiI_{5-x}Br_x$, the absorption edge shifts to larger energies, which is in agreement with an increase in band gap with increasing Br content. The resulting band gaps were estimated using Tauc plots and are listed in Table 4. The lowest band gaps were obtained for the iodine-rich compositions, with $MXDBiI_5$ exhibiting the lowest band gap in the series (2.15 eV) and $MXD_3Bi_2Br_{12}{\cdot}2H_2O$ the largest (2.86 eV). In contrast, the band gap of MXD_2PbI_6 was determined to be 2.33 eV. The variation of band gap with bromine content is shown in Figure 7b and shows an increase in band gap with increasing bromine content, although this trend is not linear. We also note that the band gap of $MXDBiI_{5-x}Br_x$ can be tuned over a similar range to that observed for the $FAPbI_{3-x}Br_x$ perovskites, which allowed tuning of the band gap from 1.48 to 2.25 eV.[3] The high crystallinity of these samples warrants further investigation into the photostability of $MXDBiI_{5-x}Br_x$, as in the mixed cation, mixed halide perovskites, $Cs_yFA_{1-y}PbI_{3-x}Br_x$, a high level of crystallinity was found to suppress halide segregation.[43]

Table 4. Bromine Content in $MXDBiI_{5-x}Br_x$ (Determined from EDS) and Corresponding Band Gap of $MXDBiI_{5-x}Br_x$ Samples

Bromine Content (x) in $MXDBiI_{5-x}Br_x$	Band Gap (eV)
0.00	2.15
0.27	2.16
0.43	2.17
0.89	2.22
1.69	2.27
2.71	2.36
3.71	2.48
$MXD_3Bi_2Br_{12}{\cdot}2H_2O$ ($x = 5$)	2.86

CONCLUSIONS

Here, we have reported the synthesis and characterization of three new organic−inorganic metal halides, using the *meta*-xylylenediammonium (MXD) cation: $MXDBiI_5$, $MXD_3Bi_2Br_{12}{\cdot}2H_2O$, and MXD_2PbI_6. $MXDBiI_5$ has short intercluster I−I distances and $\pi-\pi$ stacking between the MXD cations, while also possessing the lowest band gap of the materials studied here. We explored the tunability of $MXDBiI_5$ through halide substitution and found that a large region of solid solution exists in the $MXDBiI_{5-x}Br_x$ system (where $x = 0$ to 3.71). This work highlights the fact that zero-dimensional organic−inorganic halides are also highly tunable semiconductors and opens up the way for further studies of the physics and the long-term stability of these materials.

ASSOCIATED CONTENT

Supporting Information

The Supporting Information is available free of charge at https://pubs.acs.org/doi/10.1021/acs.cgd.2c00187.

PXRD data, SEM images, graphs of unit cell parameters, UV−vis spectra (PDF)

Accession Codes

CCDC 2151572−2151574 contain the supplementary crystallographic data for this paper. These data can be obtained free of charge via www.ccdc.cam.ac.uk/data_request/cif, or by emailing data_request@ccdc.cam.ac.uk, or by contacting The Cambridge Crystallographic Data Centre, 12 Union Road, Cambridge CB2 1EZ, UK; fax: +44 1223 336033.

AUTHOR INFORMATION

Corresponding Author

Julia L. Payne − *School of Chemistry, University of St Andrews, St Andrews, Fife KY16 9ST, United Kingdom;* orcid.org/0000-0003-3324-6018; Email: jlp8@st-andrews.ac.uk

Authors

Pia S. Klee − *School of Chemistry, University of St Andrews, St Andrews, Fife KY16 9ST, United Kingdom*

Yuri Hirano − *School of Chemistry, University of St Andrews, St Andrews, Fife KY16 9ST, United Kingdom*

David B. Cordes − *School of Chemistry, University of St Andrews, St Andrews, Fife KY16 9ST, United Kingdom;* orcid.org/0000-0002-5366-9168

Alexandra M. Z. Slawin − *School of Chemistry, University of St Andrews, St Andrews, Fife KY16 9ST, United Kingdom;* orcid.org/0000-0002-9527-6418

Complete contact information is available at: https://pubs.acs.org/10.1021/acs.cgd.2c00187

Notes

The authors declare no competing financial interest.

https://doi.org/10.1021/acs.cgd.2c00187
Cryst. Growth Des. XXXX, XXX, XXX−XXX

■ ACKNOWLEDGMENTS

J.L.P. thanks the University of St Andrews for funding and the Carnegie Trust for a Research Incentive Grant (RIG008653). We thank EPSRC for funding (EP/T019298/1 and EP/R023751/1).

■ REFERENCES

(1) Kojima, A.; Teshima, K.; Shirai, Y.; Miyasaka, T. Organometal Halide Perovskites as Visible-Light Sensitizers for Photovoltaic Cells. *J. Am. Chem. Soc.* **2009**, *131* (17), 6050−6051.

(2) Lee, M. M.; Teuscher, J.; Miyasaka, T.; Murakami, T. N.; Snaith, H. J. Efficient Hybrid Solar Cells Based on Meso-Superstructured Organometal Halide Perovskites. *Science* **2012**, *338* (6107), 643−647. Liu, M.; Johnston, M. B.; Snaith, H. J. Efficient planar heterojunction perovskite solar cells by vapour deposition. *Nature* **2013**, *501* (7467), 395−398. Jeon, N. J.; Noh, J. H.; Kim, Y. C.; Yang, W. S.; Ryu, S., Il; Seol, S. Solvent engineering for high-performance inorganic-organic hybrid perovskite solar cells. *Nat. Mater.* **2014**, *13* (9), 897−903.

(3) Eperon, G. E.; Stranks, S. D.; Menelaou, C.; Johnston, M. B.; Herz, L. M.; Snaith, H. J. Formamidinium lead trihalide: a broadly tunable perovskite for efficient planar heterojunction solar cells. *Energy Environ. Sci.* **2014**, *7* (3), 982−988.

(4) McMeekin, D. P.; Sadoughi, G.; Rehman, W.; Eperon, G. E.; Saliba, M.; Hoerantner, M. T.; Haghighirad, A.; Sakai, N.; Korte, L.; Rech, B.; et al. A mixed-cation lead mixed-halide perovskite absorber for tandem solar cells. *Science* **2016**, *351* (6269), 151−155.

(5) https://www.nrel.gov/pv/cell-efficiency.html. (accessed 23rd December 2021).

(6) Whitfield, P. S.; Herron, N.; Guise, W. E.; Page, K.; Cheng, Y. Q.; Milas, I.; Crawford, M. K. Structures, Phase Transitions and Tricritical Behavior of the Hybrid Perovskite Methyl Ammonium Lead Iodide. *Sci. Rep.* **2016**, *6*, 35685.

(7) Saparov, B.; Mitzi, D. B. Organic-Inorganic Perovskites: Structural Versatility for Functional Materials Design. *Chem. Rev.* **2016**, *116* (7), 4558−4596.

(8) Tsai, H. H.; Nie, W. Y.; Blancon, J. C.; Toumpos, C. C. S.; Asadpour, R.; Harutyunyan, B.; Neukirch, A. J.; Verduzco, R.; Crochet, J. J.; Tretiak, S.; et al. High-efficiency two-dimensional Ruddlesden-Popper perovskite solar cells. *Nature* **2016**, *536* (7616), 312−316.

(9) Sidhik, S.; Li, W. B.; Samani, M. H. K.; Zhang, H.; Wang, Y. F.; Hoffman, J.; Fehr, A. K.; Wong, M. S.; Katan, C.; Even, J.; et al. Memory Seeds Enable High Structural Phase Purity in 2D Perovskite Films for High-Efficiency Devices. *Adv. Mater.* **2021**, *33*, 2007176.

(10) Jesper Jacobsson, T.; Correa-Baena, J.-P.; Pazoki, M.; Saliba, M.; Schenk, K.; Gratzel, M.; Hagfeldt, A. Exploration of the compositional space for mixed lead halogen perovskites for high efficiency solar cells. *Energy Environ. Sci.* **2016**, *9* (5), 1706−1724.

(11) Hao, F.; Stoumpos, C. C.; Chang, R. P. H.; Kanatzidis, M. G. Anomalous Band Gap Behavior in Mixed Sn and Pb Perovskites Enables Broadening of Absorption Spectrum in Solar Cells. *J. Am. Chem. Soc.* **2014**, *136* (22), 8094−8099.

(12) Li, C.; Wei, J.; Sato, M.; Koike, H.; Xie, Z. Z.; Li, Y. Q.; Kanai, K.; Kera, S.; Ueno, N.; Tang, J. X. Halide-Substituted Electronic Properties of Organometal Halide Perovskite Films: Direct and Inverse Photoemission Studies. *ACS Appl. Mater. Int.* **2016**, *8* (18), 11526−11531.

(13) Zarick, H. F.; Soetan, N.; Erwin, W. R.; Bardhan, R. Mixed halide hybrid perovskites: a paradigm shift in photovoltaics. *J. Mater. Chem. A* **2018**, *6* (14), 5507−5537.

(14) Hoke, E. T.; Slotcavage, D. J.; Dohner, E. R.; Bowring, A. R.; Karunadasa, H. I.; McGehee, M. D. Reversible photo-induced trap formation in mixed-halide hybrid perovskites for photovoltaics. *Chem. Sci.* **2015**, *6* (1), 613−617. Slotcavage, D. J.; Karunadasa, H. I.; McGehee, M. D. Light-Induced Phase Segregation in Halide-Perovskite Absorbers. *ACS Energy Lett.* **2016**, *1* (6), 1199−1205.

(15) Hassan, Y.; Park, J. H.; Crawford, M. L.; Sadhanala, A.; Lee, J.; Sadighian, J. C.; Mosconi, E.; Shivanna, R.; Radicchi, E.; Jeong, M.; et al. Ligand-engineered bandgap stability in mixed-halide perovskite LEDs. *Nature* **2021**, *591* (7848), 72−77.

(16) Li, X. T.; Ke, W. J.; Traore, B.; Guo, P. J.; Hadar, I.; Kepenekian, M.; Even, J.; Katan, C.; Stoumpos, C. C.; Schaller, R. D.; et al. Two-Dimensional Dion-Jacobson Hybrid Lead Iodide Perovskites with Aromatic Diammonium Cations. *J. Am. Chem. Soc.* **2019**, *141* (32), 12880−12890.

(17) Gao, L.; Li, X.; Traore, B.; Zhang, Y.; Fang, J.; Yu, H.; Even, J.; Katan, C.; Zhao, K.; Liu, S.; et al. m-Phenylenediammonium as a New Spacer for Dion−Jacobson Two-Dimensional Perovskites. *J. Am. Chem. Soc.* **2021**, *143* (31), 12063−12073.

(18) Smith, I. C.; Hoke, E. T.; Solis-Ibarra, D.; McGehee, M. D.; Karunadasa, H. I. A Layered Hybrid Perovskite Solar-Cell Absorber with Enhanced Moisture Stability. *Angew. Chem., Int. Ed.* **2014**, *53* (42), 11232−11235.

(19) Pious, J. K.; Katre, A.; Muthu, C.; Chakraborty, S.; Krishna, S.; Nair, V. C. Zero-Dimensional Lead-Free Hybrid Perovskite-like Material with a Quantum-Well Structure. *Chem. Mater.* **2019**, *31* (6), 1941−1945.

(20) Ni, C. S.; Hedley, G.; Payne, J.; Svrcek, V.; McDonald, C.; Jagadamma, L. K.; Edwards, P.; Martin, R.; Jain, G.; Carolan, D.; et al. Charge carrier localised in zero-dimensional $(CH_3NH_3)_3Bi_2I_9$ clusters. *Nat. Commun.* **2017**, *8*, 170.

(21) Chatterjee, S.; Payne, J.; Irvine, J. T. S.; Pal, A. J. Bandgap bowing in a zero-dimensional hybrid halide perovskite derivative: spin-orbit coupling versus lattice strain. *J. Mater. Chem. A* **2020**, *8* (8), 4416−4427.

(22) Yin, J.; Bredas, J. L.; Bakr, O. M.; Mohammed, O. F. Boosting Self-Trapped Emissions in Zero-Dimensional Perovskite Heterostructures. *Chem. Mater.* **2020**, *32* (12), 5036−5043.

(23) Poglitsch, A.; Weber, D. Dynamic Disorder in Methylammoniumtrihalogenoplumbates (II) Observed by Millimeter-Wave Spectroscopy. *J. Chem. Phys.* **1987**, *87* (11), 6373−6378.

(24) Coelho, A. A. TOPAS and TOPAS-Academic: an optimization program integrating computer algebra and crystallographic objects written in C plus. *J. Appl. Crystallogr.* **2018**, *51*, 210−218.

(25) *CrystalClear-SM Expert ver. 2.1*; Rigaku Americas, The Woodlands, Texas, USA and Rigaku Corporation, Tokyo, Japan, 2015.

(26) *CrysAlisPro ver. 1.171.38.46, ver. 1.171.41.93a, and ver. 1.171.41.122a*; Rigaku Oxford Diffraction, Rigaku Corporation, Oxford, U.K., 2015, 2020, and 2021.

(27) Sheldrick, G. M. SHELXT - Integrated space-group and crystal-structure determination. *Acta Crystallogr., Sect. A: Found. Adv.* **2015**, *71*, 3−8.

(28) Sheldrick, G. M. Crystal structure refinement with SHELXL. *Acta Crystallogr., Sect. C: Struct. Chem.* **2015**, *71*, 3−8.

(29) Robinson, K.; Gibbs, G. V.; Ribbe, P. H. Quadriatic Elongation-Quantitative Measure of Distortion in Coordination Polyhedra. *Science* **1971**, *172* (3983), 567−570.

(30) Hrizi, C.; Trigui, A.; Abid, Y.; Chniba-Boudjada, N.; Bordet, P.; Chaabouni, S. alpha- to beta- $(C_6H_4(NH_3)_2)_2Bi_2I_{10}$ reversible solid-state transition, thermochromic and optical studies in the p-phenylenediamine-based iodobismuthate(III) material. *J. Solid State Chem.* **2011**, *184* (12), 3336−3344.

(31) Hrizi, C.; Samet, A.; Abid, Y.; Chaabouni, S.; Fliyou, M.; Koumina, A. Crystal structure, vibrational and optical properties of a new self-organized material containing iodide anions of bismuth(III), $(C_6H_4(NH_3)_2)_2Bi_2I_{10}$ center dot $4H_2O$. *J. Mol. Struct.* **2011**, *992* (1−3), 96−101.

(32) Shestimerova, T. A.; Golubev, N. A.; Yelavik, N. A.; Bykov, M. A.; Grigorieva, A. V.; Wei, Z.; Dikarev, E. V.; Shevelkov, A. V. Role of I_2 Molecules and Weak Interactions in Supramolecular Assembling of Pseudo-Three-Dimensional Hybrid Bismuth Polyiodides: Synthesis, Structure, and Optical Properties of Phenylenediammonium Polyiodobismuthate(III). *Cryst. Growth Des.* **2018**, *18* (4), 2572−2578.

https://doi.org/10.1021/acs.cgd.2c00187
Cryst. Growth Des. XXXX, XXX, XXX−XXX

(33) Guo, Y. Y.; Lightfoot, P. Structural diversity of lead halide chain compounds, $APbX_3$, templated by isomeric molecular cations. *Dalton Trans* **2020**, *49* (36), 12767−12775.
(34) Umari, P.; Mosconi, E.; De Angelis, F. Relativistic GW calculations on $CH_3NH_3PbI_3$ and $CH_3NH_3SnI_3$ Perovskites for Solar Cell Applications. *Sci. Rep.* **2015**, *4*, 4467.
(35) Mosconi, E.; Amat, A.; Nazeeruddin, M. K.; Gratzel, M.; De Angelis, F. First-Principles Modeling of Mixed Halide Organometal Perovskites for Photovoltaic Applications. *J. Phys. Chem. C* **2013**, *117* (27), 13902−13913.
(36) Yin, J.; Maity, P.; De Bastiani, M.; Dursun, I.; Bakr, O. M.; Bredas, J. L.; Mohammed, O. F. Molecular behavior of zero-dimensional perovskites. *Sci. Adv.* **2017**, *3* (12), 1701793. Almutlaq, J.; Yin, J.; Mohammed, O. F.; Bakr, O. M. The Benefit and Challenges of Zero-Dimensional Perovskites. *J. Phys. Chem. Lett.* **2018**, *9* (14), 4131−4138.
(37) Stoumpos, C. C.; Cao, D. H.; Clark, D. J.; Young, J.; Rondinelli, J. M.; Jang, J. I.; Hupp, J. T.; Kanatzidis, M. G. Ruddlesden-Popper Hybrid Lead Iodide Perovskite 2D Homologous Semiconductors. *Chem. Mater.* **2016**, *28*, 2852−2867.
(38) Karim, M. M. S; Ganose, A. M.; Pieters, L.; Leung, W. W. W.; Wade, J.; Zhang, L.; Scanlon, D. O.; Palgrave, R. G. Anion Distribution, Structural Distortion, and Symmetry-Driven Optical Band Gap Bowing in Mixed Halide Cs_2SnX_6 Vacancy Ordered Double Perovskites. *Chem. Mater.* **2019**, *31* (22), 9430−9444.
(39) Shannon, R. D. Revised effective ionic radii and systematic studies of interatomic distances in halides and chalcogenides. *Acta Crystallogr., Sect. A: Found. Adv.* **1976**, *32*, 751−767.
(40) Sheikh, T.; Shinde, A.; Mahamuni, S.; Nag, A. Possible Dual Bandgap in $(C_4H_9NH_3)_2PbI_4$ 2D Layered Perovskite: Single-Crystal and Exfoliated Few-Layer. *ACS Energy Lett.* **2018**, *3* (12), 2940−2946. Lyu, D.; Miao, Y.; Li, B. Y.; Xiao, Z. Q.; Wu, X.; Hu, X. W.; Jiang, X. F.; Xu, Q. H. Dual Blue Emission in Ruddlesden-Popper Lead-Bromide Perovskites Induced by Photon Recycling. *J. Phys. Chem. C* **2021**, *125* (33), 18308−18316.
(41) Nawale, V. V.; Sheikh, T.; Nag, A. Dual Excitonic Emission in Hybrid 2D Layered Tin Iodide Perovskites. *J. Phys. Chem. C* **2020**, *124* (38), 21129−21136.
(42) Peng, H.; Tian, Y.; Wang, X. X.; Huang, T.; Xiao, Y. H.; Dong, T. T.; Hu, J. M.; Wang, J. P.; Zou, B. S. Bulk assembly of a 0D organic antimony chloride hybrid with highly efficient orange dual emission by self-trapped states. *J. Mater. Chem. C* **2021**, *9* (36), 12184−12190.
(43) Rehman, W.; McMeekin, D. P.; Patel, J. B.; Milot, R. L.; Johnston, M. B.; Snaith, H. J.; Herz, L. M. Photovoltaic mixed-cation lead mixed-halide perovskites: links between crystallinity, photo-stability and electronic properties. *Energy Environ. Sci.* **2017**, *10* (1), 361−369.

https://doi.org/10.1021/acs.cgd.2c00187
Cryst. Growth Des. XXXX, XXX, XXX−XXX